

Small Models, Strong Priors: Architectural Inductive Bias for Parameter-Efficient Neural PDE Solvers

Shyam Sankaran

Department of Mechanical Engineering and Applied Mechanics, University of Pennsylvania
shyamss@seas.upenn.edu

Hanwen Wang

Graduate Program in Applied Mathematics and Computational Science, University of Pennsylvania
wangh19@sas.upenn.edu

Paris Perdikaris

Department of Mechanical Engineering and Applied Mechanics, University of Pennsylvania
pgp@seas.upenn.edu

Abstract

Neural PDE solvers have followed the scaling trajectory of vision and language, with recent foundation models reaching billions of parameters. We argue that scale is a poor substitute for architectural inductive bias in this domain: structured priors deliver outsized parameter efficiency, and the pattern of where they succeed and fail is itself informative about what they capture. We instantiate this argument in *WaveLiT*, an architecture combining a discrete wavelet transform for lossless multi-resolution tokenization, an augmented linear attention block, a shared-weight multiscale feature pyramid, and a wavelet-domain auxiliary loss. Bespoke 1–10M-parameter *WaveLiT* models compete with foundation models of 100–1000 \times their size across eight TheWell benchmarks, with the largest gains on wave- and acoustic-dominated benchmarks where the wavelet-multiscale prior fits the dominant dynamical structure and small per-step errors do not compound geometrically under rollout. Trained jointly across all eight benchmarks, a 10M-parameter foundation variant exhibits a structured, physically interpretable transfer pattern – strongest where the wavelet-multiscale prior matches the dynamics, weakest on chaotic advection-dominated flows. The entire pipeline trains on a single GPU. The results suggest that small-model PDE performance is shaped by architectural inductive bias rather than scale, and that the structure of a prior’s failures is a useful empirical signal about its content.

1 Introduction

Neural surrogates for partial differential equations are increasingly central to scientific computing, with applications spanning weather forecasting [5], fluid dynamics, and materials science [45]. The promise is straightforward: where classical solvers cost hours per simulation, learned surrogates cost milliseconds. Realizing this promise at the accuracy required for scientific use has, in current practice, driven the field toward ever-larger models.

Preprint.

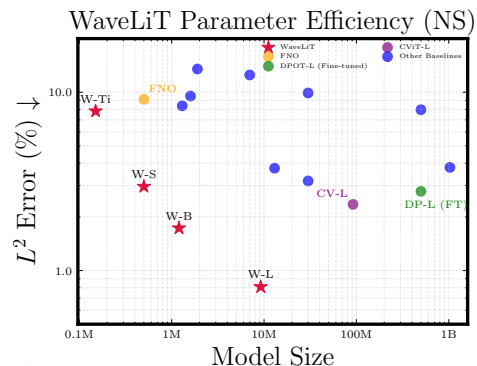


Figure 1: Parameter efficiency on PDEArena Navier-Stokes [13]. Each point is a model; lower-left is better. *WaveLiT* (red stars) outperforms models with 100 \times more parameters.

Following the scaling regimes established in language [23] and vision [50], neural PDE solvers have moved from thousands of parameters to billions. Recent foundation models such as PhysiX (4.5B) [35], DPOT (500M) [15], Poseidon (629M) [17], and Walrus (1.2B) [34] pursue general-purpose simulators by combining massive parameter counts with multi-task training across diverse PDE families. Training these models requires hundreds of GPU-hours and infrastructure that is inaccessible to most research groups.

At the same time, the broader ML community is increasingly recognizing that scale is not the only axis of progress. Compact language models have emerged as efficient backbones for downstream systems [1, 4], demonstrating that careful architectural and data choices can substitute for raw parameter count. A complementary direction in reasoning has shown that small networks with appropriate inductive structure – HRM at 27M parameters [43] and TRM at 7M [22] – can be competitive on tasks with exploitable combinatorial structure. Neural PDE solvers occupy an analogous setting: the underlying physics imposes locality, regularity, and multi-scale structure that should, in principle, be exploitable by smaller models, yet architectural defaults in this field have not been re-examined under this lens.

Most current PDE models inherit their design from vision transformers, adopting defaults that were never optimized for physical systems. Coarse 8×8 or 16×16 patch tokenization discards sub-patch physics before the first attention layer, and quadratic self-attention forces this coarse tokenization by making fine-grained alternatives prohibitively expensive. These defaults interact in a vicious cycle: quadratic attention demands fewer tokens, which demands coarser patches, which destroys fine-scale physics, which demands more parameters to compensate.

We introduce *WaveLiT*, an integrated architecture that addresses each of these defaults. A discrete wavelet transform replaces learned patch embedding with parameter-free, lossless multi-resolution tokenization. A linear attention block with $\mathcal{O}(N)$ complexity replaces quadratic self-attention, building on Mamba-Inspired Linear Attention [14] and the test-time-regression view of attention [41, 3] adapted to the bidirectional spatial setting. A shared-weight multiscale feature pyramid processes tokens at multiple resolutions without adding parameters, and a wavelet-domain auxiliary loss encourages spectral fidelity across scales.

These choices compound into a parameter-efficient frontier (Figure 1). On PDEArena Navier-Stokes [13], WaveLiT matches or exceeds FNO [27], CViT-L [47], and DPOT-L [15] at 10–100× fewer parameters; on TheWell [36], bespoke 1–10M-parameter models compete with foundation-model baselines (MPP-AViT-L, Poseidon-L, DPOT-H, Walrus) of 100–1000× their size, with the largest gains on wave- and acoustic-dominated benchmarks. To probe whether these architectural priors survive cross-family training, we use the foundation-model regime as a diagnostic instrument: a single 10M-parameter model trained jointly on all eight TheWell benchmarks exhibits a structured, physically interpretable transfer pattern – strongest where the wavelet-multiscale prior matches the dynamics, weakest on chaotic advection-dominated flows. The entire pipeline trains on a single GPU. We do not claim global SOTA against billion-parameter specialists; we claim that the recipe defines an efficient frontier, and that the structure of its successes and failures provides evidence that small-model PDE performance is shaped by inductive bias, not scale alone.

2 Related Work

Neural operators for PDEs. Neural operators approximate mappings between infinite-dimensional function spaces [26], with two main paradigms: encoder-decoder operators such as DeepONet [31] and NoMaD [37], which map functions to latent spaces and back; and integral kernel operators [25] parameterized via graph message passing [28] or Fourier transforms [27]. These methods established that operator-valued targets can be learned end-to-end, but typically at single resolution and without explicit multi-scale structure — the property our design is built to exploit.

Vision transformers for operator learning. ViTs [12] have been adapted to operator learning, most prominently by CViT [47], which combines ViT encoders with coordinate embeddings and cross-attention. These approaches inherit two defaults from vision: quadratic-cost softmax attention and coarse patch tokenization. The two interact: quadratic attention forces large patches to keep sequence lengths tractable, and large patches discard the fine-scale physics that PDE solutions actually

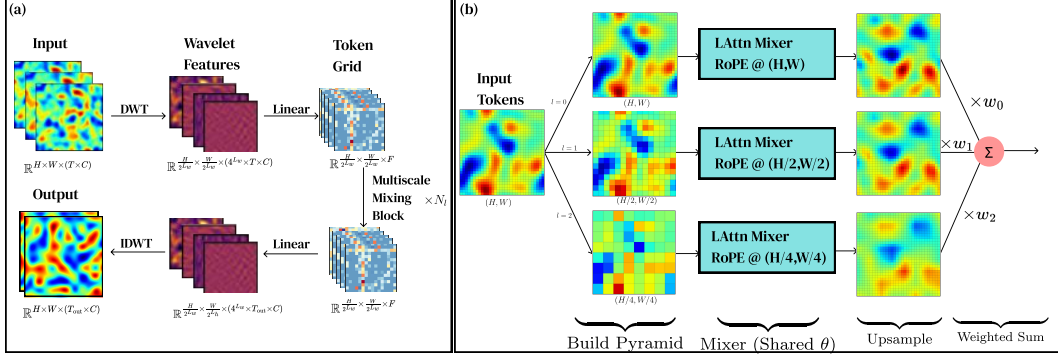


Figure 2: The *WaveLiT* architecture: (a) Input fields are tokenized via a single-level 2D discrete wavelet transform (DWT), projected to embedding dimension via a linear layer, and processed by N_L multiscale mixing blocks. The output is recovered by a final linear projection and inverse DWT, restoring the original spatial resolution. (b) Each multiscale mixing block applies a shared-weight linear attention mixer at $L + 1$ resolutions obtained by successive average pooling. Per-level RoPE frequencies are calibrated to each grid size; outputs are upsampled to the base resolution and combined via learned scalar weights w_ℓ

depend on. *WaveLiT* removes both defaults simultaneously — linear attention enables fine-grained tokens, and a wavelet transform supplies them losslessly.

Efficient sequence modeling. Linear attention [24] reduces the $\mathcal{O}(N^2)$ cost of softmax attention to $\mathcal{O}(N)$. Recent work has reframed such mechanisms through a test-time regression lens: DeltaNet [49] frames the recurrent state update as gradient descent on a per-token MSE loss, and the test-time-regression perspective [44, 3] shows that many modern sequence models can be derived from specific regression objectives. We adopt the Mamba-Inspired Linear Attention block [14] as a starting point and develop a ridge-corrected variant motivated by this perspective (§3), specifically adapted to the bidirectional, spatially-tokenized setting of grid-structured PDE data – a regime that prior linear-attention work has largely targeted only in causal sequence settings.

Wavelets in deep learning. Wavelet transforms decompose signals into components localized jointly in space and frequency, providing a principled framework for multi-resolution analysis [32, 18]. In deep learning, wavelets have been used for image compression [2] and as a tokenization scheme for vision transformers [51]. Within operator learning, Wavelet Neural Operators perform kernel integration in the wavelet domain [40], and Wavelet Diffusion Neural Operators apply diffusion-based modeling in the wavelet domain for PDE simulation and control [21]. Our use of wavelets is distinct: we use the DWT not as the substrate for a specialized operator, but as a parameter-free tokenization that preserves multi-scale structure end-to-end through a transformer backbone, with the wavelet domain reused as an auxiliary loss to enforce spectral fidelity.

Foundation models for physics simulation. The field has shifted toward general-purpose “foundation models” that aim to solve a diverse range of PDE problems [35, 17, 15], with recent entries reaching billions of parameters: Walrus at 1.2B [34], PhysiX at 4.5B [35]. These models achieve strong benchmark results but require infrastructure inaccessible to most research groups, and the implicit hypothesis – that scale is what makes cross-family transfer possible – has not been tested against architecturally efficient alternatives. Our foundation-model variant is designed precisely as such a test: at 10M parameters, memorization is mechanically infeasible, so any cross-family transfer that does occur must come from shared architectural priors.

3 Architecture

WaveLiT is an integrated architecture for neural PDE solvers built around four components: discrete wavelet tokenization, a gated linear attention block, a shared-weight multiscale feature pyramid, and a wavelet-domain auxiliary loss. Each component targets a specific architectural default inherited from vision transformers that we identified in Section 1. We describe each in turn, then describe the foundation-model extension *WaveLiT-FM*. Figure 2 summarizes the architecture.

3.1 Wavelet Tokenization

We replace the standard patch embedding with a single-level 2D discrete wavelet transform (DWT). The DWT decomposes each spatial field into four half-resolution subbands (one low-frequency approximation LL and three directional detail bands LH , HL , HH), yielding the same $4\times$ channel expansion and $2\times$ spatial reduction as a 2×2 patch projection but with three key advantages: the transform is (i) *lossless*, admitting exact reconstruction via the inverse DWT; (ii) *physically meaningful*, separating large-scale structure from edges and directional textures; and (iii) *parameter-free*, supplying an inductive bias with no learnable weights. For inputs of shape $B\times T\times H\times W\times C$, an ℓ -level DWT produces tokens of shape $B\times T\times (H/2^\ell)\times (W/2^\ell)\times (C\cdot 4^\ell)$; a linear projection then maps the concatenated subbands to the model dimension. We use $\ell = 1$ throughout to preserve fine-grained features at the input layer; this choice is consistent with recent findings that smaller patch sizes outperform parameter scaling in sub-quadratic vision architectures at fixed compute [42]. We use the `bior2.2` wavelet throughout (ablations in Appendix C) and apply the inverse DWT at the output to recover the original resolution.

In practice, wavelet tokenization yields a modest accuracy gain over a convolutional encoder-decoder (+1.4%) while reducing training time by 11%, consistent with the finding of [20] in a diffusion setting; the inductive bias primarily provides efficiency rather than a large accuracy jump. Full tokenizer ablations are in Appendix I.

3.2 Spatial Linear Attention Mixer

On high-resolution grids, the $\mathcal{O}(N^2)$ cost of softmax self-attention quickly becomes prohibitive. We therefore replace quadratic attention with a kernelized linear attention operator whose cost scales linearly in the number of tokens. Let $\phi(\cdot)$ denote a positive feature map applied to queries and keys. The output at token i can then be written as

$$o_i = S\phi(q_i), \quad S = \sum_{j=1}^N v_j\phi(k_j)^\top, \quad (1)$$

where the state $S \in \mathbb{R}^{d_v \times d_k}$ is accumulated once and reused across all query locations. This reordering removes the quadratic dependence on the number of tokens while preserving global token mixing.

Ridge-corrected state update. We additionally apply a ridge-corrected variant of the state update, $S_\lambda = C(G + \lambda I)^{-1}$ with $C = \sum_j v_j\phi(k_j)^\top$ and $G = \sum_j \phi(k_j)\phi(k_j)^\top$, which can be motivated through the test-time regression view of linear attention [41, 3] as incorporating the covariance structure of the kernel features. Full derivation in Appendix A; ablations (Appendix I.2) indicate this provides incremental rather than dominant gains relative to the spatial inductive biases described next.

Additional Spatial Inductive Biases. While linear attention addresses the computational bottleneck, it does not by itself provide a strong spatial inductive bias for dense grid-structured data. To remedy this, we adopt an MILA-style mixer design that augments linear attention with positional operators tailored to vision-like inputs. Concretely, we apply rotary positional embeddings [38] (RoPE) to the query/key feature maps, use conditional positional encoding (CPE) [7] as a depthwise-convolutional positional term on the residual stream before the attention and MLP sub-blocks, and add locally enhanced positional encoding (LePE) [11] as a depthwise-convolutional local bias on the attention output path. This combination injects both global positional structure and local spatial bias while preserving linear-time token mixing. This design is motivated by recent MILA results showing that, in vision settings, suitable positional encodings can effectively replace forget-gate-like functionality while retaining parallelizable computation [14].

Our final mixer combines these ingredients into a single block: RoPE-equipped linear attention for efficient global token interaction, a ridge-corrected state update motivated by the regression view above, and an MILA-style block design with CPE and LePE to supply the spatial inductive bias required on high-resolution grids. In practice, we use this full configuration throughout the model. We study the effect of the individual design choices and their relative contributions in Appendix I.2.

3.3 Multiscale Computation

PDE solutions exhibit structure across spatial scales. Rather than only relying on network depth to capture cross-scale interactions, we process information at multiple resolutions using a feature-pyramid structure [29] with shared parameters.

Given input tokens $X \in \mathbb{R}^{B \times N \times D}$ on a grid of size (H, W) , we construct a resolution pyramid $\{X^{(\ell)}\}_{\ell=0}^L$ by successive $2 \times$ average pooling. A shared-weight linear attention block f_θ is applied at each level:

$$Y^{(\ell)} = f_\theta(X^{(\ell)}, g^{(\ell)}), \quad (2)$$

where $g^{(\ell)}$ encodes the grid size at level ℓ for positional embeddings. Outputs are upsampled and aggregated via learned scalar weights:

$$\hat{X} = \sum_{\ell} w_{\ell} \cdot \text{Upsample}(Y^{(\ell)}). \quad (3)$$

Weight sharing provides multiscale sensitivity without increasing parameters; coarse levels process far fewer tokens, making additional levels computationally cheap. Concurrent work applies a similar resolution-pyramid strategy with shared attention weights for PDE simulation, achieving linear complexity via a multipole analogy [8]; our design differs in using average pooling for downsampling and learned scalar weights for aggregation. A single pyramid level reduces error by 17.4% over wavelet-only tokenization at 16% additional training cost; additional levels yield diminishing returns. We use $L = 1$ throughout; full ablations across tokenizer and FPN depth are in Appendix I.

3.4 Wavelet-Domain Auxiliary Loss

The wavelet basis used for tokenization also defines a natural multi-scale loss. In addition to a pixel-space MSE loss on predicted fields, we apply an L_1 loss in the wavelet domain: predictions and targets are both DWT-transformed, and the absolute error is summed across all subbands. This encourages the model to match high-frequency detail coefficients as well as low-frequency approximations, which the MSE loss alone tends to underweight. Appendix D reports an ablation showing that the auxiliary loss reduces error power across the entire spatial-frequency spectrum.

3.5 Foundation-Model Extension: WaveLiT-FM

WaveLiT-FM extends the bespoke architecture to joint training across all eight TheWell benchmarks. The key additions over the single-task design, illustrated in Figure 3, are a per-channel lifting embedding that gates absent fields to zero, a per-dataset task conditioning vector, and per-dataset output heads.

Unified input representation. We define a canonical channel space of dimension C_{total} by taking the union of all unique physical variables (e.g., u -velocity, pressure, buoyancy, tracer) across TheWell. Each dataset maps its available fields to their designated canonical channels and zero-pads the rest. Channel identity is encoded through a per-channel lifting matrix $W_{\text{lift}} \in \mathbb{R}^{C_{\text{total}} \times T n_{\text{bands}} \times D}$: after the wavelet decomposition, each channel’s coefficients are projected independently and summed, $\mathbf{z} = \sum_c \mathbf{x}_c W_{\text{lift}}[c]$. Because there is no bias term, absent (zero-padded) channels contribute exactly zero to the embedding — the shared trunk receives a representation that is naturally gated by which fields are present. Channels shared across datasets (e.g., u -velocity in both `shear_flow` and `rayleigh_benard`) reuse the same rows of W_{lift} , encouraging a common latent representation for each physical field type.

Task-specific conditioning. After the initial linear projection, we add a learnable per-dataset embedding vector to every token. This informs the shared trunk which PDE system it is solving without breaking weight sharing.

Shared backbone. The wavelet embedding, MILA stack, and reconstruction layer serve as a shared trunk trained jointly on all eight datasets; per-task specialization is confined entirely to the task-conditioning vector and output head, with no dataset-specific parameters in the core computation.

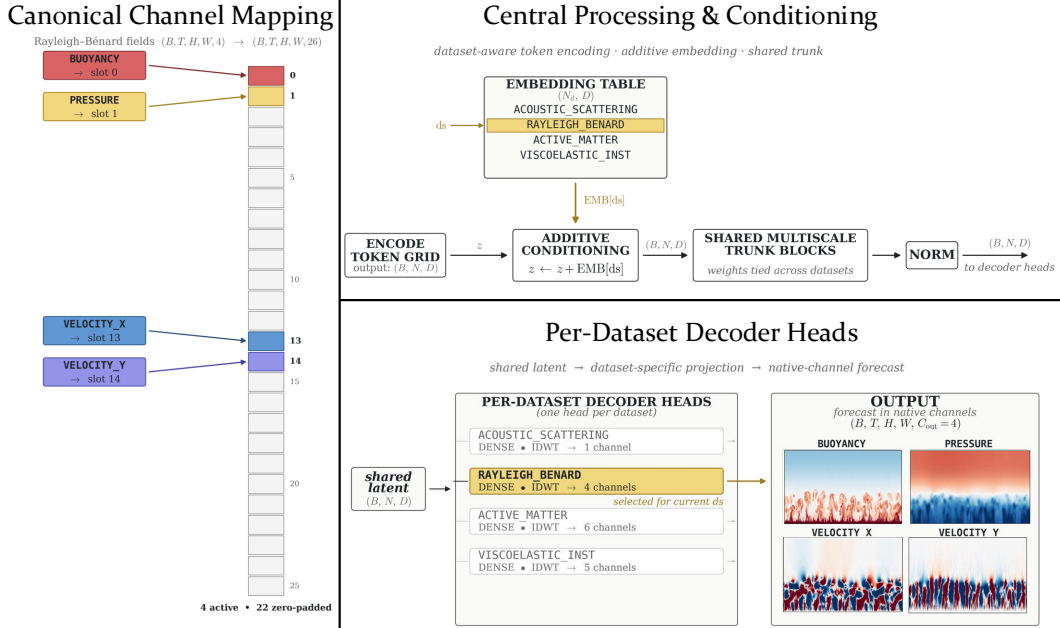


Figure 3: Foundation model design: (i) input standardization via a per-channel lifting matrix without bias, so absent (zero-padded) channels contribute exactly zero to the trunk input; (ii) problem-embedding conditioning of a shared multiscale transformer trunk; and (iii) per-dataset decoder heads decoding the shared latent representation into native output channels.

Specialized output heads. Each dataset has a separate lightweight linear head that decodes the final shared latent representation into its specific output channels. The head contributes negligible parameters relative to the trunk.

4 Results

4.1 Bespoke Models: Parameter Efficiency

Implementation details. We train two model sizes (1.2M and 9.5M parameters) on each TheWell benchmark separately using AdamW [30] with exponential learning rate decay and gradient clipping. Both variants use a single-level DWT tokenization, the combined MSE and wavelet loss (Section 3.4), and exponential parameter averaging at evaluation. We additionally train rollout-finetuned (FT) variants by continuing from the pretrained checkpoint with an autoregressive rollout objective to improve long-horizon stability. Our rollout-finetuning protocol and the comparison that motivates it are detailed in Appendix G. All training is performed in JAX [6]/Flax [16] on a single GPU; full hyperparameters are in Appendix E.

We report each model’s median VRMSE normalized to the per-dataset best baseline. WaveLiT bespoke models match or exceed foundation-model baselines with 100–1000× more parameters (Figure 4; absolute VRMSE in Appendix J). We compare against MPP-AViT-L (409M) [33], Poseidon-L (629M) [17], DPOT-H (~1B) [15], and Walrus (1.2B) [34].

One-step prediction (panel a). Averaged across the eight TheWell benchmarks, WaveLiT-9.5M ranks as the second-best model in the one-step regime with a mean per-dataset rank of 1.94, trailing only Walrus (1.44) and outperforming all other foundation-model (FM) baselines. Remarkably, even WaveLiT-1.2M—a model ~1000× smaller than Walrus—outperforms the remaining three FM baselines, achieving a mean rank of 3.12 compared to Poseidon-L (4.12), MPP-AViT-L (4.86), and DPOT-H (5.38) (Table 18). On the two wave- and acoustic-dominated benchmarks, ASM and HS, our architecture achieves state-of-the-art results despite its size. Specifically, WaveLiT-9.5M outperforms every baseline including Walrus on ASM (0.0016 vs. 0.0099), and WaveLiT-1.2M achieves the same feat on HS (0.0003 vs. 0.0005). Across the remaining six datasets, WaveLiT consistently surpasses

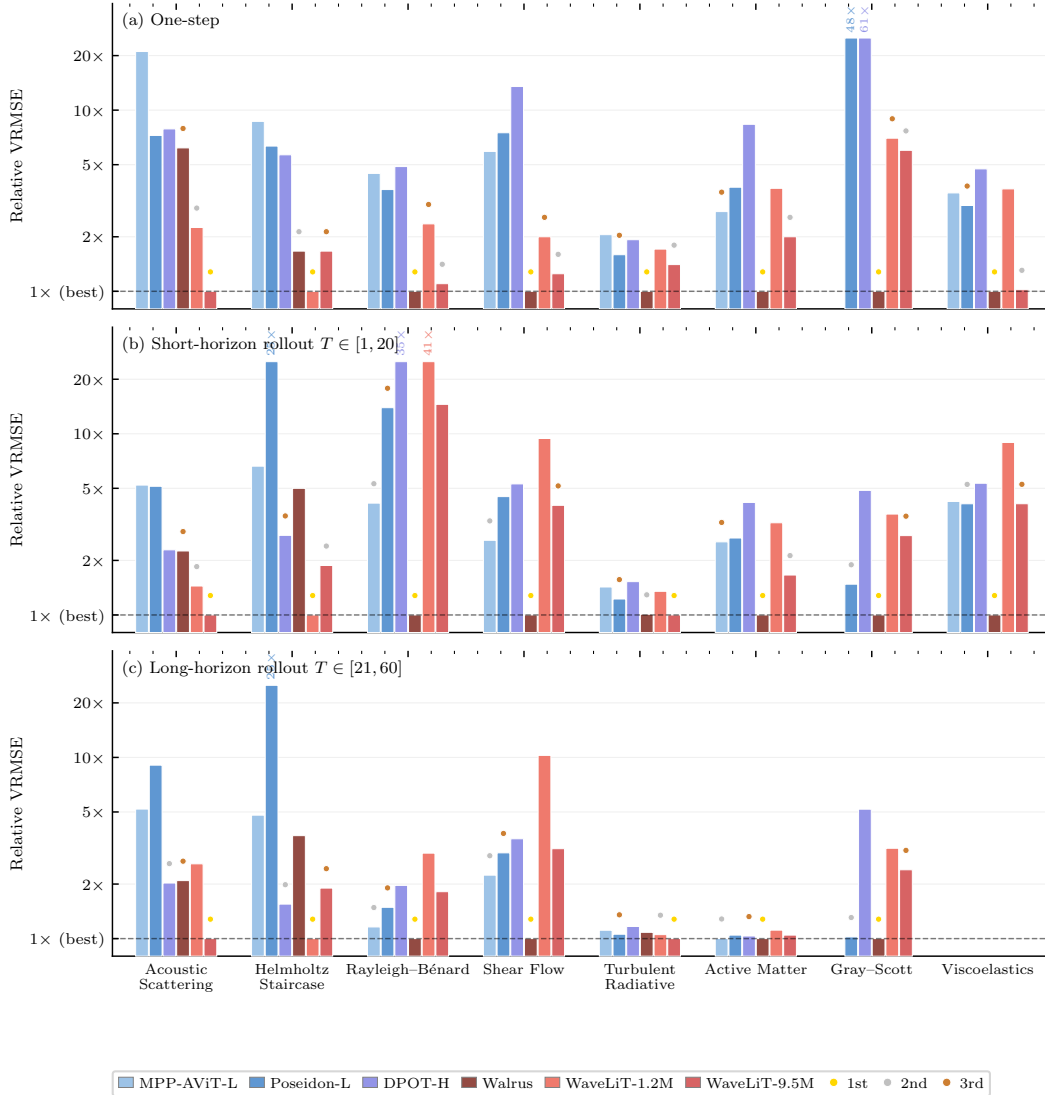


Figure 4: WaveLiT bespoke models vs. foundation model baselines across eight TheWell benchmarks and three evaluation windows, normalized per dataset to the best model ($1\times = \text{best}$, log scale). Each WaveLiT bar shows the better of pretrained and rollout-finetuned variants. Gold, silver, and bronze markers denote the top three results per benchmark. Absolute VRMSE values and full PT/FT breakdown in Appendix J.

MPP-AViT-L, Poseidon-L, and DPOT-H. The performance gap to Walrus remains narrow on RB, SF, and VI, but widens on TRL2D, AM, and GS, where Walrus’s billion-parameter capacity and design likely provide a decisive advantage.

Longer rollouts (panels b, c). However, this initial one-step advantage does not carry uniformly to longer rollouts. WaveLiT-9.5M’s mean rank degrades from 1.94 at one-step to 2.38 at $T \in [1, 20]$ and 3.00 at $T \in [21, 60]$, with Walrus’ margin widening accordingly (Table 18). When the learned map has a local Lipschitz constant $L_F > 1$, the per-step error ϵ accumulates as $\epsilon(L_F^n - 1)/(L_F - 1)$. Rollout finetuning does not reduce ϵ in isolation; rather, it trades ϵ against L_F . This trade-off is consistent with the worse one-step accuracy of our finetuned (FT) variants relative to their pre-trained (PT) counterparts (Appendix H). On chaotic dynamics, L_F is bounded below by $e^{\lambda\Delta t}$, where λ is the leading Lyapunov exponent of the underlying flow and Δt is the time step; geometric error growth therefore survives finetuning. Consequently, our long-horizon wins occur on non-chaotic systems

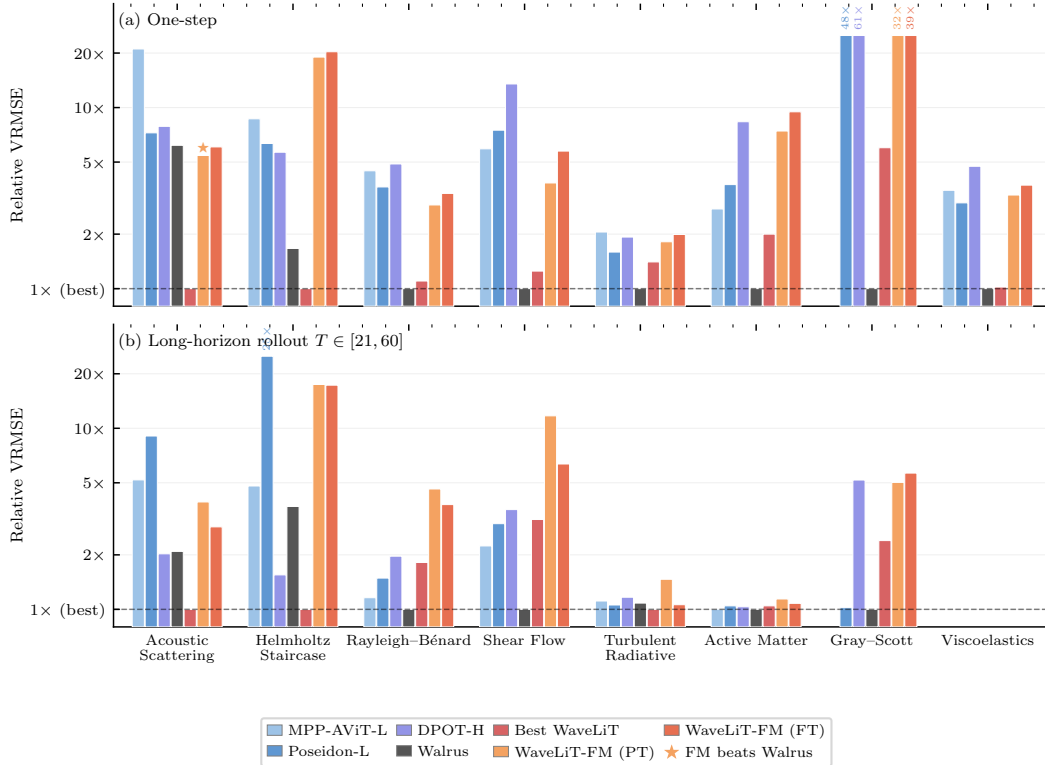


Figure 5: Foundation model diagnostic. Relative VRMSE (normalized per dataset to the best model; $1 \times = \text{best}$, log scale) for all four baselines, the best bespoke WaveLiT, and both WaveLiT-FM variants. ★ marks the one cell where a multi-task model (Fnd-PT on ASM, one-step) outperforms Walrus.

where $L_F \leq 1$, such as ASM (9.5M-FT: 0.0268 vs. Walrus 0.0560) and HS (1.2M-PT: 0.0020 vs. DPOT-H 0.0031). Conversely, evolution on RB is dominated by fine-scale structures that inherently drive $L_F > 1$, causing both our models to diverge under rollout.¹

4.2 Foundation Model Diagnostic

WaveLiT-FM is a 10M-parameter model trained jointly across all eight TheWell benchmarks on a single GPU, using the shared-backbone design of Section 3.5 with \sqrt{N} -proportional dataset sampling. It is not designed to maximize benchmark performance; it is a diagnostic instrument for whether the architectural priors survive cross-family training. Figure 5 compares Walrus, the best bespoke WaveLiT variant, and both FM variants (pretrained and rollout-finetuned) at one-step and long-horizon rollout; full tables are in Appendix J.

Summary of Results. At one-step on ASM, both multi-task variants fall below Walrus (0.0099): Fnd-PT (0.0087, ★) and Fnd-FT (0.0097). Together with Fnd-FT on TRL2D at long horizon (0.8471 vs. Walrus 0.8648), these are the only three cells in this comparison where a multi-task model beats Walrus. Overall, the FM’s performance gap relative to the bespoke WaveLiT ceiling is modest on most datasets (RB and SF $\sim 3 \times$, ASM and GS $\sim 5 \times$), with one pronounced exception: HS, where it widens to $19 \times$.

Pattern of transfer. The FM’s degradation relative to bespoke is structured. HS shows by far the largest relative degradation under shared-trunk training ($19 \times$ at one-step). It is the dataset where the bespoke specialist achieved its lowest absolute error (0.0003) by aggressively exploiting dataset-specific structure, and joint training forces a shared, generalized basis that blurs the hyper-specific

¹The 9.5M-FT RB checkpoint uses early stopping at 40k steps; the final 50k checkpoint diverges further. The 1.2M-FT checkpoint exhibits the same instability without recovery from earlier checkpoints.

filters it depends on. Conversely, datasets where bespoke and Walrus performance were already comparable (ASM, RB, TRL2D) show much smaller relative gaps. Ultimately, the FM inherits the bespoke model’s strengths and weaknesses in proportion to how well the inductive bias aligns with the local dynamics. This suggests that future scaling of WaveLiT-FM should prioritize specialized per-dataset sampling for complex flows rather than merely increasing backbone capacity. Furthermore, our current joint training relies on static \sqrt{N} -proportional sampling, meaning the model’s exposure to each dataset is fixed by volume rather than task difficulty. A promising direction for future work is the development of an adaptive sampling strategy that dynamically adjusts batch composition based on the evolution of validation loss, potentially recovering the specialization lost in standard multi-task training.

An observation on transfer. A valuable outcome of running identical architectures in both regimes is the rare opportunity to directly compare their performance dynamics. Within our experimental setup, joint training across diverse PDE families did not yield positive transfer; rather, it consistently diluted specialization. Across all eight TheWell datasets, the bespoke WaveLiT specialists outperformed the multi-task FM variant, sometimes by over an order of magnitude. At this compact scale of 10M parameters, we did not anticipate strong positive transfer, as the network likely lacks the sheer capacity required to represent multiple disjoint physical manifolds simultaneously without severe interference. This raises a fascinating open question: does unlocking synergistic benefits between fundamentally different PDE families strictly require billion-parameter backbones? Currently, these mechanisms are difficult to isolate, as many pioneering PDE foundation models [34, 17, 15, 35] are evaluated primarily as unified systems without bespoke single-task ablations of their own backbones. Our results do not settle this question, but they do raise it: the implicit assumption that multi-PDE pretraining transfers benefits to individual tasks deserves explicit experimental support.

5 Discussion

Summary of findings. Bespoke WaveLiT models (1–10M parameters) can match or exceed foundation models up to $1000\times$ larger, particularly on smooth problems where our inductive bias perfectly aligns with the underlying physics. On chaotic datasets, this prior improves one-step accuracy but cannot bypass the instability of teacher-forced rollouts. Crucially, our 10M-parameter WaveLiT-FM diagnostic model exhibits the exact same performance patterns as the single-task specialists. At this scale, brute-force memorization is impossible, confirming that multi-task transfer behavior is driven by the architectural prior rather than sheer scale.

Limitations & Future Directions. Our primary limitation is autoregressive instability on chaotic dynamics, driven by fundamental mathematical bounds rather than training budgets. Under rollout, per-step error ϵ and the local Lipschitz constant L_F dictate error growth: $E_n \leq \epsilon(L_F^n - 1)/(L_F - 1)$ (Appendix H). Rollout finetuning trades ϵ against L_F , but it cannot suppress L_F below $e^{\lambda\Delta t}$, where λ is the leading Lyapunov exponent of the system; thus, geometric growth is unavoidable. Furthermore, resolving chaotic, high-frequency subbands inherently increases L_F , making our fine-grained tokenization a double-edged sword. A coarser patch embedding that never represents those modes yields a smaller effective L_F and slower error growth, sacrificing one-step accuracy for potentially better long-term stability. Addressing this requires migrating from static, single-step maps to architectures equipped with strong temporal mechanisms. Immediate mitigations include temporal noise injection, or “jitter,” as leveraged by Walrus [34]. More fundamentally, incorporating temporal linear attention would allow the model to propagate a continuous hidden state, naturally regularizing the rollout trajectory. Extending this architecture to complex geometries via lifting wavelets [39] is a natural next step.

Conclusions. WaveLiT demonstrates that combining lossless multi-resolution tokenization with linear attention and shared-weight multiscale processing yields a parameter-efficient design competitive with foundation models $100\text{--}1000\times$ larger on the PDE families where its prior matches the underlying physics. Beyond the architecture, the results provide a data point on the inductive-bias-versus-scale question: at scales where memorization is mechanically infeasible, cross-family transfer is shaped by the structure of the prior, and the pattern of failures is physically legible.

References

- [1] Marah Abdin, Jyoti Aneja, Harkirat Behl, Sébastien Bubeck, Ronen Eldan, Suriya Gunasekar, Michael Harrison, Russell J Hewett, Mojan Javaheripi, Piero Kauffmann, et al. Phi-4 technical report. *arXiv preprint arXiv:2412.08905*, 2024.
- [2] Tinku Acharya and Ping-Sing Tsai. *JPEG2000 standard for image compression: concepts, algorithms and VLSI architectures*. John Wiley & Sons, 2004.
- [3] Ali Behrouz, Meisam Razaviyayn, Peilin Zhong, and Vahab Mirrokni. It’s all connected: A journey through test-time memorization, attentional bias, retention, and online optimization. *arXiv preprint arXiv:2504.13173*, 2025.
- [4] Peter Belcak, Greg Heinrich, Shizhe Diao, Yonggan Fu, Xin Dong, Saurav Muralidharan, Yingyan Celine Lin, and Pavlo Molchanov. Small language models are the future of agentic ai. *arXiv preprint arXiv:2506.02153*, 2025.
- [5] Cristian Bodnar, Wessel P Bruinsma, Ana Lucic, Megan Stanley, Johannes Brandstetter, Patrick Garvan, Maik Riechert, Jonathan Weyn, Haiyu Dong, Anna Vaughan, et al. Aurora: A foundation model of the atmosphere. *arXiv preprint arXiv:2405.13063*, 2024.
- [6] James Bradbury, Roy Frostig, Peter Hawkins, Matthew James Johnson, Chris Leary, Dougal Maclaurin, George Necula, Adam Paszke, Jake VanderPlas, Skye Wanderman-Milne, and Qiao Zhang. JAX: composable transformations of Python+NumPy programs, 2018.
- [7] Xiangxiang Chu, Zhi Tian, Bo Zhang, Xinlong Wang, and Chunhua Shen. Conditional positional encodings for vision transformers. *arXiv preprint arXiv:2102.10882*, 2021.
- [8] Alex Colagrande, Paul Caillon, Eva Feillet, and Alexandre Allauzen. Linear attention with global context: A multipole attention mechanism for vision and physics. In *Proceedings of the IEEE/CVF International Conference on Computer Vision*, pages 3099–3108, 2025.
- [9] Alexis Conneau, Kartikay Khandelwal, Naman Goyal, Vishrav Chaudhary, Guillaume Wenzek, Francisco Guzmán, Edouard Grave, Myle Ott, Luke Zettlemoyer, and Veselin Stoyanov. Unsupervised cross-lingual representation learning at scale. In *Proceedings of the 58th annual meeting of the association for computational linguistics*, pages 8440–8451, 2020.
- [10] Katherine Crowson. jax-wavelets: The 2D discrete wavelet transform for JAX, 2022.
- [11] Xiaoyi Dong, Jianmin Bao, Dongdong Chen, Weiming Zhang, Nenghai Yu, Lu Yuan, Dong Chen, and Baining Guo. Cswin transformer: A general vision transformer backbone with cross-shaped windows. In *Proceedings of the IEEE/CVF conference on computer vision and pattern recognition*, pages 12124–12134, 2022.
- [12] Alexey Dosovitskiy, Lucas Beyer, Alexander Kolesnikov, Dirk Weissenborn, Xiaohua Zhai, Thomas Unterthiner, Mostafa Dehghani, Matthias Minderer, Georg Heigold, Sylvain Gelly, et al. An image is worth 16x16 words: Transformers for image recognition at scale. *arXiv preprint arXiv:2010.11929*, 2020.
- [13] Jayesh K Gupta and Johannes Brandstetter. Towards multi-spatiotemporal-scale generalized pde modeling. *arXiv preprint arXiv:2209.15616*, 2022.
- [14] Dongchen Han, Ziyi Wang, Zhuofan Xia, Yizeng Han, Yifan Pu, Chunjiang Ge, Jun Song, Shiji Song, Bo Zheng, and Gao Huang. Demystify mamba in vision: A linear attention perspective. *arXiv preprint arXiv:2405.16605*, 2024.
- [15] Zhongkai Hao, Chang Su, Songming Liu, Julius Berner, Chengyang Ying, Hang Su, Anima Anandkumar, Jian Song, and Jun Zhu. Dpot: Auto-regressive denoising operator transformer for large-scale pde pre-training. *arXiv preprint arXiv:2403.03542*, 2024.
- [16] Jonathan Heek, Anselm Levskaya, Avital Oliver, Marvin Ritter, Bertrand Rondepierre, Andreas Steiner, and Marc van Zee. Flax: A neural network library and ecosystem for JAX, 2024.

- [17] Maximilian Herde, Bogdan Raonic, Tobias Rohner, Roger Käppeli, Roberto Molinaro, Emmanuel de Bézenac, and Siddhartha Mishra. Poseidon: Efficient foundation models for pdes. *Advances in Neural Information Processing Systems*, 37:72525–72624, 2024.
- [18] Eugenio Hernández and Guido Weiss. *A first course on wavelets*. CRC press, 1996.
- [19] Geoffrey E Hinton and James A Anderson. *Parallel models of associative memory: updated edition*. Psychology press, 2014.
- [20] Emiel Hoogeboom, Jonathan Heek, and Tim Salimans. simple diffusion: End-to-end diffusion for high resolution images. In *International Conference on Machine Learning*, pages 13213–13232. PMLR, 2023.
- [21] Peiyan Hu, Rui Wang, Xiang Zheng, Tao Zhang, Haodong Feng, Ruiqi Feng, Long Wei, Yue Wang, Zhi-Ming Ma, and Tailin Wu. Wavelet diffusion neural operator. *arXiv preprint arXiv:2412.04833*, 2024.
- [22] Alexia Jolicoeur-Martineau. Less is more: Recursive reasoning with tiny networks. *arXiv preprint arXiv:2510.04871*, 2025.
- [23] Jared Kaplan, Sam McCandlish, Tom Henighan, Tom B Brown, Benjamin Chess, Rewon Child, Scott Gray, Alec Radford, Jeffrey Wu, and Dario Amodei. Scaling laws for neural language models. *arXiv preprint arXiv:2001.08361*, 2020.
- [24] Angelos Katharopoulos, Apoorv Vyas, Nikolaos Pappas, and François Fleuret. Transformers are rnns: Fast autoregressive transformers with linear attention. In *International conference on machine learning*, pages 5156–5165. PMLR, 2020.
- [25] Nikola Kovachki, Zongyi Li, Burigede Liu, Kamyar Azizzadenesheli, Kaushik Bhattacharya, Andrew Stuart, and Anima Anandkumar. Neural operator: Learning maps between function spaces with applications to pdes. *Journal of Machine Learning Research*, 24(89):1–97, 2023.
- [26] Nikola B Kovachki, Samuel Lanthaler, and Andrew M Stuart. Operator learning: Algorithms and analysis. *arXiv preprint arXiv:2402.15715*, 2024.
- [27] Zongyi Li, Nikola Kovachki, Kamyar Azizzadenesheli, Burigede Liu, Kaushik Bhattacharya, Andrew Stuart, and Anima Anandkumar. Fourier neural operator for parametric partial differential equations. *arXiv preprint arXiv:2010.08895*, 2020.
- [28] Zongyi Li, Nikola Kovachki, Kamyar Azizzadenesheli, Burigede Liu, Kaushik Bhattacharya, Andrew Stuart, and Anima Anandkumar. Neural operator: Graph kernel network for partial differential equations. *arXiv preprint arXiv:2003.03485*, 2020.
- [29] Tsung-Yi Lin, Piotr Dollár, Ross Girshick, Kaiming He, Bharath Hariharan, and Serge Belongie. Feature pyramid networks for object detection. In *Proceedings of the IEEE conference on computer vision and pattern recognition*, pages 2117–2125, 2017.
- [30] Ilya Loshchilov and Frank Hutter. Decoupled weight decay regularization. *arXiv preprint arXiv:1711.05101*, 2017.
- [31] Lu Lu, Pengzhan Jin, Guofei Pang, Zhongqiang Zhang, and George Em Karniadakis. Learning nonlinear operators via deepnet based on the universal approximation theorem of operators. *Nature machine intelligence*, 3(3):218–229, 2021.
- [32] Stephane G Mallat. A theory for multiresolution signal decomposition: the wavelet representation. *IEEE transactions on pattern analysis and machine intelligence*, 11(7):674–693, 1989.
- [33] Michael McCabe, Bruno Régalo-Saint Blancard, Liam Holden Parker, Ruben Ohana, Miles Cranmer, Alberto Bietti, Michael Eickenberg, Siavash Golkar, Geraud Krawezik, Francois Lanusse, et al. Multiple physics pretraining for physical surrogate models. *arXiv preprint arXiv:2310.02994*, 2023.

- [34] Michael McCabe, Payel Mukhopadhyay, Tanya Marwah, Bruno Regaldo-Saint Blancard, Francois Rozet, Cristiana Diaconu, Lucas Meyer, Kaze WK Wong, Hadi Sotoudeh, Alberto Bietti, et al. Walrus: A cross-domain foundation model for continuum dynamics. *arXiv preprint arXiv:2511.15684*, 2025.
- [35] Tung Nguyen, Arsh Koneru, Shufan Li, and Aditya Grover. Physix: A foundation model for physics simulations. *arXiv preprint arXiv:2506.17774*, 2025.
- [36] Ruben Ohana, Michael McCabe, Lucas Meyer, Rudy Morel, Fruzsina Agocs, Miguel Beneitez, Marsha Berger, Blakesly Burkhart, Stuart Dalziel, Drummond Fielding, et al. The well: a large-scale collection of diverse physics simulations for machine learning. *Advances in Neural Information Processing Systems*, 37:44989–45037, 2024.
- [37] Jacob Seidman, Georgios Kissas, Paris Perdikaris, and George J Pappas. Nomad: Nonlinear manifold decoders for operator learning. *Advances in Neural Information Processing Systems*, 35:5601–5613, 2022.
- [38] Jianlin Su, Murtadha Ahmed, Yu Lu, Shengfeng Pan, Wen Bo, and Yunfeng Liu. Roformer: Enhanced transformer with rotary position embedding. *Neurocomputing*, 568:127063, 2024.
- [39] Wim Sweldens. The lifting scheme: A construction of second generation wavelets. *SIAM journal on mathematical analysis*, 29(2):511–546, 1998.
- [40] Tapas Tripura and Souvik Chakraborty. Wavelet neural operator: a neural operator for parametric partial differential equations. *arXiv preprint arXiv:2205.02191*, 2022.
- [41] Johannes von Oswald, Nino Scherrer, Seijin Kobayashi, Luca Versari, Songlin Yang, Maximilian Schlegel, Kaitlin Maile, Yanick Schimpf, Oliver Sieberling, Alexander Meulemans, et al. Mesanet: Sequence modeling by locally optimal test-time training. *arXiv preprint arXiv:2506.05233*, 2025.
- [42] Feng Wang, Yaodong Yu, Guoyizhe Wei, Wei Shao, Yuyin Zhou, Alan Yuille, and Cihang Xie. Scaling laws in patchification: An image is worth 50,176 tokens and more. *arXiv preprint arXiv:2502.03738*, 2025.
- [43] Guan Wang, Jin Li, Yuhao Sun, Xing Chen, Changling Liu, Yue Wu, Meng Lu, Sen Song, and Yasin Abbasi Yadkori. Hierarchical reasoning model. *arXiv preprint arXiv:2506.21734*, 2025.
- [44] Ke Alexander Wang, Jiaxin Shi, and Emily B Fox. Test-time regression: a unifying framework for designing sequence models with associative memory. *arXiv preprint arXiv:2501.12352*, 2025.
- [45] Sifan Wang, Tong-Rui Liu, Shyam Sankaran, and Paris Perdikaris. Micrometer: Micromechanics transformer for predicting mechanical responses of heterogeneous materials. *arXiv preprint arXiv:2410.05281*, 2024.
- [46] Sifan Wang, Shyam Sankaran, and Paris Perdikaris. Respecting causality is all you need for training physics-informed neural networks. *arXiv preprint arXiv:2203.07404*, 2022.
- [47] Sifan Wang, Jacob H Seidman, Shyam Sankaran, Hanwen Wang, George J Pappas, and Paris Perdikaris. Cvit: Continuous vision transformer for operator learning. *arXiv preprint arXiv:2405.13998*, 2024.
- [48] Linting Xue, Noah Constant, Adam Roberts, Mihir Kale, Rami Al-Rfou, Aditya Siddhant, Aditya Barua, and Colin Raffel. mt5: A massively multilingual pre-trained text-to-text transformer. In *Proceedings of the 2021 conference of the North American chapter of the association for computational linguistics: Human language technologies*, pages 483–498, 2021.
- [49] Songlin Yang, Jan Kautz, and Ali Hatamizadeh. Gated delta networks: Improving mamba2 with delta rule. *arXiv preprint arXiv:2412.06464*, 2024.
- [50] Xiaohua Zhai, Alexander Kolesnikov, Neil Houlsby, and Lucas Beyer. Scaling vision transformers. In *Proceedings of the IEEE/CVF conference on computer vision and pattern recognition*, pages 12104–12113, 2022.

- [51] Zhenhai Zhu and Radu Soricut. Wavelet-based image tokenizer for vision transformers. *arXiv preprint arXiv:2405.18616*, 2024.

A Linear Attention and the Ridge Regression View

From softmax to linear attention. Standard attention computes $\text{Attn}(Q, K, V) = \text{softmax}(QK^\top/\sqrt{d})V$, whose QK^\top matrix is $N \times N$ and makes both memory and compute scale quadratically with sequence length. Any positive-definite kernel $\kappa(q, k)$ admits a feature-map factorization $\kappa(q, k) = \langle \phi(q), \phi(k) \rangle$; replacing the softmax with such a factorization gives

$$o_i = \frac{\sum_j \phi(q_i)^\top \phi(k_j) v_j}{\sum_j \phi(q_i)^\top \phi(k_j)}. \quad (4)$$

Because $\phi(q_i)$ appears only as a left-multiplier, we can reorder the computation: accumulate $S = \sum_j v_j \phi(k_j)^\top \in \mathbb{R}^{d_v \times d_k}$ once, then evaluate $o_i = S \phi(q_i)$ for each query. This reduces complexity to $\mathcal{O}(N)$ [24]. We follow common practice and omit the denominator, which many architectures drop without significant performance loss, giving

$$o_i = S \phi(q_i), \quad S = \sum_{j=1}^N v_j \phi(k_j)^\top. \quad (5)$$

RNN interpretation. The state $S \in \mathbb{R}^{d_v \times d_k}$ accumulates key-value associations and is queried via a dot product — it functions as an associative memory [19]. Under causal (left-to-right) ordering, S is updated token-by-token: $S_i = S_{i-1} + v_i \phi(k_i)^\top$, giving an exact equivalence with an RNN whose hidden state is matrix-valued. For our setting — bidirectional spatial attention over PDE grids — S is accumulated over all tokens simultaneously, but the $\mathcal{O}(N)$ cost and fixed-size state are retained.

A.1 The Ridge Regression View

The accumulated state S in (5) can be given an optimization interpretation. Consider the Frobenius-regularized reconstruction loss

$$\min_S \left[\sum_{j=1}^N \|v_j - S \phi(k_j)\|^2 + \lambda \|S\|_F^2 \right]. \quad (6)$$

Setting the gradient to zero yields the closed-form solution

$$S^* = \left(\sum_j v_j \phi(k_j)^\top \right) (G + \lambda I)^{-1}, \quad G = \sum_j \phi(k_j) \phi(k_j)^\top. \quad (7)$$

The three regularization regimes connect directly to known architectures [44, 3, 41]:

Regime	Solution	Interpretation
$\lambda \gg \ G\ $	$\lambda^{-1} \sum_j v_j \phi(k_j)^\top$	Vanilla linear attention (5)
Finite λ	$\left(\sum_j v_j \phi(k_j)^\top \right) (G + \lambda I)^{-1}$	Ridge-corrected (WaveLiT)
$\lambda \rightarrow 0$	$\left(\sum_j v_j \phi(k_j)^\top \right) G^{-1}$	Least-squares

In the large- λ regime, $(G + \lambda I)^{-1} \approx \lambda^{-1} I$ and the Gram correction vanishes — all feature directions are treated as equally important regardless of how frequently they are queried. The scalar λ^{-1} is absorbed into the output projection during training, leaving the functional form of vanilla linear attention (5). Vanilla linear attention thus corresponds to *ignoring the covariance structure* of the key features entirely. WaveLiT uses a finite- λ ridge correction, incorporating the Gram matrix G to account for how frequently each direction in feature space is queried. The correction adds a matrix inverse of size $d_k \times d_k$, which is cheap when $d_k \ll N$. Ablations comparing vanilla, ridge-corrected, and least-squares variants are in Appendix I.2.

B Impact of Sequence Length and Attention Mechanism on Performance and Efficiency

We explore the interplay between model architecture, effective sequence length (modulated by wavelet decomposition levels), and computational cost.

Scope of this comparison. The study presented here isolates the choice of *token-mixing primitive* (DPA versus MILA) and is intended only to motivate the move away from $\mathcal{O}(N^2)$ self-attention in long-sequence wavelet-tokenized inputs. The configurations evaluated below predate the full WaveLiT mixer and do *not* include ridge regularization and gating. The accuracy numbers should therefore be read as a baseline-vs-baseline comparison of attention kernels, not as the performance of WaveLiT itself; ablations of the full mixer recipe are reported separately in Appendix I. We retain this earlier comparison because the compute/accuracy trade-off it exposes between DPA and MILA is the original motivation for our linear-attention design choice and remains informative on its own.

Our primary goal is to identify model configurations that balance high accuracy with manageable computational cost. We compare standard Dot-Product Attention (DPA) with an enhanced linear attention mechanism (MILA) [14]. To understand these trade-offs, we conducted evaluations on the Navier-Stokes (NS) benchmark from PDEArena [13], following the experimental setup established in DPOT [15]. We compared models using both DPA and MILA across different model sizes (“WaveLiT-1.2M” vs. “WaveLiT-9.5M”) and wavelet decomposition levels (1 vs. 2 levels, where fewer levels mean longer effective sequences). The results, including relative L_2 error and training time per 1000 iterations, are presented in Table 1 and visualized for key configurations in Figure 6. While detailed results are shown for NS, similar trends in the DPA vs. MILA trade-off were observed across other datasets.

Table 1: Performance and efficiency comparison of Dot-Product Attention (DPA) and Enhanced Linear Attention (MILA) across varying model sizes and wavelet levels. Training time is per 1000 iterations.

Attention	Model	Wavelet Levels	Params (M)	Training Time (s)	Relative L_2
DPA	WaveLiT-9.5M	1	≈ 8.5	212.80	0.00458
MILA	WaveLiT-9.5M	1	≈ 8.5	60.00	0.00480
DPA	WaveLiT-9.5M	2	≈ 8.7	26.68	0.00711
MILA	WaveLiT-9.5M	2	≈ 8.7	15.00	0.00750
DPA	WaveLiT-1.2M	1	≈ 1.1	53.30	0.01848
MILA	WaveLiT-1.2M	1	≈ 1.1	18.00	0.01950
DPA	WaveLiT-1.2M	2	≈ 1.2	7.12	0.02606
MILA	WaveLiT-1.2M	2	≈ 1.2	5.00	0.02700

Discussion. The data in Table 1 (visualized in Figures 6 and 7) reveals several key trends regarding model performance and efficiency. Firstly, for a given model size and attention type, decreasing the number of wavelet levels (thus increasing effective sequence length) generally improves performance (lower relative L_2 error), albeit at a higher computational cost, especially for DPA. Secondly, increasing model parameters (e.g., from WaveLiT-1.2M to WaveLiT-9.5M) also tends to enhance performance. However, as detailed in Appendix E, input sequence length (determined by wavelet levels) often plays a more decisive role than raw parameter count alone, particularly for smaller models.

Most critically, these results highlight the compelling advantages of MILA. While DPA occasionally achieves marginally lower error, MILA consistently delivers comparable accuracy at a substantially reduced computational cost. For instance, with WaveLiT-9.5M and 1 wavelet level, MILA trains over 3.5 times faster than DPA for a very small trade-off in error. Therefore, MILA emerges as a highly practical and scalable attention mechanism. It allows leveraging the performance benefits of longer effective sequences, crucial for resolving fine-scale features in PDE solutions, without incurring the prohibitive computational costs.

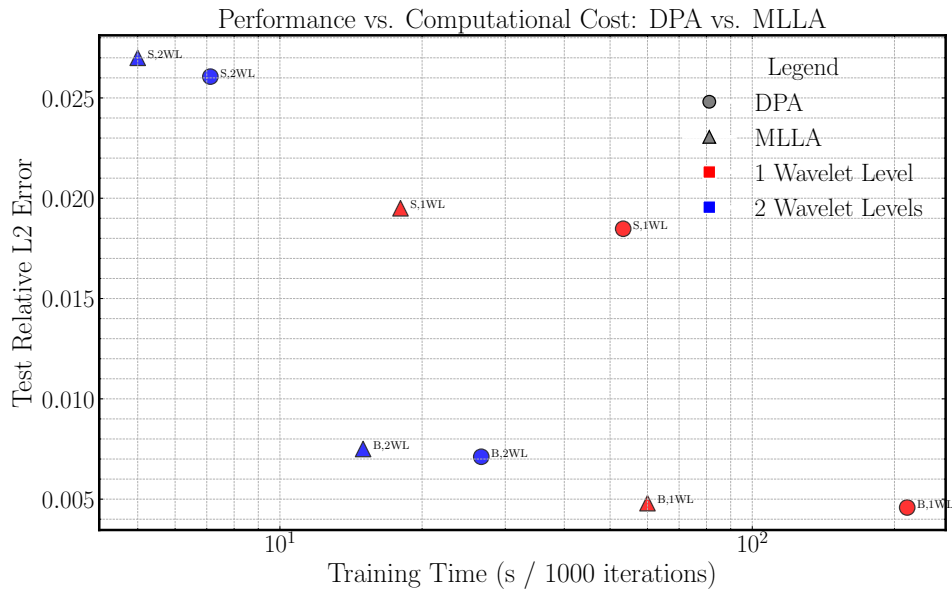


Figure 6: MLLA models (triangles) demonstrate significantly lower compute costs for comparable performance levels, especially at 1 wavelet level (longer sequences), compared to DPA models (circles)

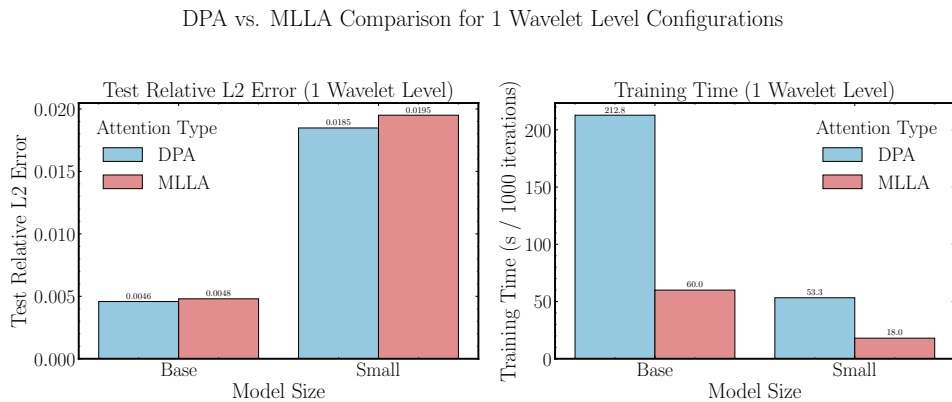


Figure 7: Comparative performance of Dot-Product Attention (DPA) and Enhanced Linear Attention (MLLA) for 1-wavelet-level (long sequence) configurations. *Left:* Test Relative L2 Error. *Right:* Training Time (sec/1000 iterations). MLLA demonstrates significant reductions in training time while maintaining competitive error rates compared to DPA across all model sizes.

C Wavelet Selection Choice

For the core experiments in this work, the Biorthogonal wavelet `bior2.2` was selected as the default choice for the wavelet transform layer. The `bior2.2` wavelet offers a good balance of properties, including symmetry and relatively compact support (filter length of 6), making it suitable for capturing features across various scales without excessive computational overhead.

To validate this choice and assess the model’s robustness to the specific wavelet employed, we conducted an ablation study. We evaluated the performance of the WaveLiT-1.2M model on the Navier-Stokes benchmark dataset provided by PDEArena [13] using three distinct wavelets: `haar`, `bior2.2`, and `bior4.4`. These wavelets represent a range of characteristics: `haar` is the simplest, discontinuous orthogonal wavelet (filter length 2); `bior2.2` is our chosen symmetric biorthogonal wavelet (filter length 6); and `bior4.4` is a smoother, higher-order symmetric biorthogonal wavelet (filter length 10). Our wavelet selection was guided by the `jax-wavelets` library [10], specifically choosing from families compatible with reflect padding, which we found to yield better performance than wrap padding in our experiments.

Discussion. The performance was measured using the relative- L_2 error for 1-step ahead predictions and 4-step rollouts. The results, presented in Table 2, demonstrate consistency across the different wavelet choices. This minimal variation in performance across wavelets with differing characteristics suggested that our architecture is reasonably robust to the specific choice of wavelet and we stick to the use of `bior2.2` as the default choice.

Table 2: Ablation study on wavelet choice for the WaveLiT-1.2M model on the Navier-Stokes benchmark. Reported values are relative- L_2 error for 1-step ahead and 4-step rollout predictions. Lower is better.

Wavelet	1-Step Ahead	4-Step Rollout
<code>haar</code>	0.010669	0.023265
<code>bior2.2</code>	0.010618	0.023349
<code>bior4.4</code>	0.010896	0.023718

D Loss Term Ablations

Table 3 presents the results of experiments investigating the impact of different loss term weightings on model performance, specifically comparing Mean Squared Error (MSE) loss and an L_1 wavelet loss (L_1 wavelet). The experiments were conducted for two model sizes (Small (1.2M) and Base (9.5M)) and two different numbers of wavelet decomposition levels (1 and 2).

Table 3: Effect of MSE and L1 Wavelet Loss Terms on Model Performance. Performance metrics are relative L_2 error on the test set for single-step prediction (Test Rel. L_2) and 4-step rollout (Test Rel. L_2 Rollout). Best results for each ablation are highlighted in bold.

Model	Wavelet Levels	Loss Weights		Test Performance	
		λ_{MSE}	λ_{L1}	Rel. L_2	Rel. L_2 Rollout (4 steps)
WaveLiT-9.5M	1	0	1	0.00416	0.01028
WaveLiT-9.5M	1	1	1	0.00453	0.01009
WaveLiT-9.5M	1	1	0	0.00563	0.01295
WaveLiT-9.5M	2	0	1	0.00662	0.01634
WaveLiT-9.5M	2	1	1	0.00670	0.01636
WaveLiT-9.5M	2	1	0	0.00837	0.01972
WaveLiT-1.2M	1	0	1	0.01177	0.02792
WaveLiT-1.2M	1	1	1	0.01167	0.02702
WaveLiT-1.2M	1	1	0	0.01280	0.02945
WaveLiT-1.2M	2	0	1	0.01407	0.03283
WaveLiT-1.2M	2	1	1	0.01406	0.03295
WaveLiT-1.2M	2	1	0	0.01515	0.03369

Discussion A clear trend emerges from the data: the inclusion of the L_1 wavelet loss term, either exclusively ($\lambda_{L1} = 1, \lambda_{MSE} = 0$) or in conjunction with the MSE loss ($\lambda_{L1} = 1, \lambda_{MSE} = 1$), consistently yields superior performance compared to using only the MSE loss ($\lambda_{L1} = 0, \lambda_{MSE} = 1$). This benefit of the wavelet loss is further demonstrated by examining the spectral characteristics of the prediction error. Figure 8 shows the Radially Averaged Power Spectral Density (RAPSD) of the prediction error for the WaveLiT-9.5M model (1 wavelet level) when trained with the combined MSE and L_1 wavelet loss versus MSE loss alone. The plot indicates that the incorporation of the wavelet loss term leads to a reduction in error power across the entire frequency spectrum compared to the model trained without it. This reduction is evident at low frequencies, corresponding to large-scale structures, and extends to higher frequencies, representing finer details. Such broad spectral improvement suggests that the L_1 wavelet loss aids the model in more accurately resolving the multi-scale features inherent in the solution.

Given these observations, we find that setting both $\lambda_{MSE} = 1$ and $\lambda_{L1} = 1$ provides robust, high-quality results. Therefore, for all experiments in this paper, we adopted this balanced weighting, setting both the MSE loss weight and the L_1 wavelet loss weight to 1.

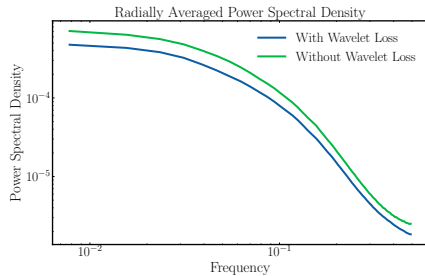


Figure 8: Radially Averaged Power Spectral Density (RAPSD) of the prediction error for the WaveLiT-9.5M model (1 wavelet level), comparing training with both MSE and L_1 wavelet loss terms (“With Wavelet Loss”) versus training with MSE loss alone (“Without Wavelet Loss”). The inclusion of the wavelet loss demonstrably reduces error power across all frequencies.

E Training Details

All models are trained using the AdamW optimizer [30], using a weight decay rate of 1×10^{-4} . We employ an exponential decay learning rate scheduler with a linear warm-up phase: the learning rate is linearly scaled up from 1×10^{-7} to 1×10^{-3} over the first 5,000 steps, after which it is exponentially decayed with a decay rate of 0.99 every 2,000 transition steps. To ensure training stability, gradients are globally clipped to a norm of 1. The batch size is set to 4 for all benchmarks. We default to a Discrete Wavelet Transform (DWT) level of 1 for most benchmarks to maximize input sequence length and provide the model with fine-grained details.

Table 4 outlines the projected total training times for 500,000 steps for various WaveLiT models across different benchmarks, without intermediate evaluation. It is important to note that these times are estimates from running on a shared NVIDIA H200 server and can vary depending on factors such as data loading efficiency, software library versions, and computational facility workload; thus, they may not perfectly and consistently reflect the raw computational cost. Table 5 shows the timings training the foundation model backbone on an NVIDIA B200.

Table 4: **Estimated bespoke model training time per dataset (GPU-hours, single GPU)**. PT times estimated as $t_{\text{iter}} \times 500,000$; FT times as $t_{\text{iter}} \times 50,000$, where t_{iter} is the mean per-iteration wall-clock time logged during training.

Dataset	Pretrain (500k iters)		Finetune (50k iters)	
	1.2M	9.5M	1.2M	9.5M
RB	5.5h	15.3h	3.3h	11.1h
ASM	5.3h	12.5h	3.3h	11.1h
SF	18.1h	25.7h	5.9h	20.2h
AM	6.9h	15.0h	4.4h	11.6h
HS	13.2h	38.3h	9.6h	38.3h
GS	2.2h	4.9h	1.4h	4.0h
VI	27.1h	42.7h	12.7h	39.6h
TRL2D	5.3h	8.9h	2.7h	8.9h
Total	83.5h	163.4h	43.3h	144.6h

Bespoke grand total: 434.8 GPU-hours (18.1 GPU-days)

Table 5: **Foundation model training time (GPU-hours, single GPU)**. PT estimated as $t_{\text{iter}} \times 1,000,000$; FT as $t_{\text{iter}} \times 50,000$. Actual wall-clock time from wandb shown in parentheses for reference.

	Pretrain (1M iters)	Finetune (50k iters)
Foundation model	41.0h (51.1h)	8.4h (8.5h)
Total	49.4 GPU-hours (2.1 GPU-days)	

Table 6: **Total compute budget summary.**

Model family	GPU-hours	GPU-days
Bespoke 1.2M (PT + FT)	126.8h	5.3
Bespoke 9.5M (PT + FT)	308.0h	12.8
Foundation (PT + FT)	49.4h	2.1
Grand total	484.2h	20.2

F Dataset Sampling Strategy

Training a shared-trunk foundation model across heterogeneous PDE datasets introduces a fundamental tension: the eight datasets in our corpus differ in size by up to $66\times$ in effective token count (Table 7). The trunk must accumulate useful gradient signal from every PDE family, yet unconstrained training will concentrate update mass on whichever datasets dominate the corpus.

Table 7 reports, for each dataset, the number of training trajectories, the native spatial resolution ($H \times W$), the effective post-wavelet token count per example ($h/2 \times w/2$ for one decomposition level), and the resulting total epoch token count $N_i = n_i \cdot \tau_i$ that serves as the basis for all sampling calculations.

Table 7: Dataset statistics. n_i : training trajectories; τ_i : tokens per example after one wavelet level (spatial dims halved); N_i : total epoch tokens. The token corpus spans nearly two orders of magnitude.

Dataset	n_i	$H \times W$	τ_i	N_i (tokens)
active_matter	14,000	256×256	16,384	229,376,000
gray_scott_reaction_diffusion	960,000	128×128	4,096	3,932,160,000
rayleigh_benard	278,600	512×128	16,384	4,564,582,400
shear_flow	178,304	256×512	32,768	5,842,665,472
turbulent_radiative_layer_2D	7,200	128×384	12,288	88,473,600
viscoelastic_instability	6,487	512×512	65,536	425,132,032
acoustic_scattering_maze	321,600	256×256	16,384	5,269,094,400
helmholtz_staircase	20,384	1024×256	65,536	1,335,885,824
Total	—	—	—	21,687,369,728

F.1 Three Candidate Sampling Schemes

Let $p_i = N_i / \sum_j N_j$ denote the proportional share of the corpus. We compare three methods for assigning the sampling probability w_i (the probability of drawing the next mini-batch from dataset i).

Uniform. $w_i = 1/K$ for all i , with $K = 8$.

Proportional, temperature $T = 0.2$.

$$w_i \propto \exp\left(\frac{p_i}{T}\right). \tag{8}$$

With $T \rightarrow 0$ all weight concentrates on $\arg \max_i p_i$; with $T \rightarrow \infty$ the scheme recovers uniform. $T = 0.2$ sharpens toward the larger datasets relative to uniform. We choose this relaxation to allow sampling from sparser datasets such as `turbulent_radiative_layer_2D` which would otherwise be sampled at less than 1% under naive proportional sampling.

\sqrt{N} -proportional.

$$w_i = \frac{\sqrt{N_i}}{\sum_j \sqrt{N_j}}. \tag{9}$$

No temperature hyperparameter; w_i lies between the pure-proportional and uniform extremes by construction.

Table 8 lists the resulting probabilities under all three schemes alongside the raw proportional share p_i for reference. Table 9 provides the most informative view: the oversampling ratio w_i/p_i , i.e., how many times more frequently each dataset is sampled relative to what its token share alone would dictate.

F.2 Analysis

We analyze the three sampling strategies based on their theoretical properties and empirical performance: Under uniform sampling, the smallest dataset (TRL2D) is drawn $30.6\times$ more often than

Table 8: Sampling probabilities under each scheme. *Prop. (pure)* is the raw token share p_i , shown for reference only.

Dataset	Prop. (pure)	Uniform	Prop. ($T=0.2$)	\sqrt{N}
active_matter	0.0106	0.1250	0.0617	0.0420
gray_scott_rd	0.1813	0.1250	0.1448	0.1737
rayleigh_benard	0.2105	0.1250	0.1676	0.1871
shear_flow	0.2694	0.1250	0.2250	0.2117
turb. rad. layer 2D	0.0041	0.1250	0.0597	0.0261
viscoelastic_inst.	0.0196	0.1250	0.0645	0.0571
acoustic_scattering	0.2430	0.1250	0.1971	0.2011
helmholtz_staircase	0.0616	0.1250	0.0796	0.1012
$D_{\text{KL}}(w_i p_i)$ [nats]	0.000	0.766	0.214	0.099

Table 9: Oversampling ratio w_i/p_i under each scheme. A ratio > 1 means the dataset is sampled more often than its raw token share warrants; ratio < 1 means it is downsampled. Pure proportional gives ratio 1.0 by definition (shown for reference).

Dataset	Prop. (pure)	Uniform	Prop. ($T=0.2$)	\sqrt{N}
active_matter	1.0 \times	11.8 \times	5.8 \times	4.0 \times
gray_scott_rd	1.0 \times	0.7 \times	0.8 \times	1.0 \times
rayleigh_benard	1.0 \times	0.6 \times	0.8 \times	0.9 \times
shear_flow	1.0 \times	0.5 \times	0.8 \times	0.8 \times
turb. rad. layer 2D	1.0 \times	30.6\times	14.6 \times	6.4\times
viscoelastic_inst.	1.0 \times	6.4 \times	3.3 \times	2.9 \times
acoustic_scattering	1.0 \times	0.5 \times	0.8 \times	0.8 \times
helmholtz_staircase	1.0 \times	2.0 \times	1.3 \times	1.6 \times

its token share warrants. This would cause overfitting on small datasets early in training. The temperature-scaled scheme partially corrects this, dropping the maximum oversampling ratio to 14.6 \times . However, this requires careful tuning of the hyper-parameter T and is dependent on the specific corpus distribution, requiring retuning if datasets are added or removed. We adopt \sqrt{N} -proportional sampling for the foundation model. It resolves the tensions of multi-physics training without introducing sensitive hyperparameters, offering distinct advantages:

- **Minimal Distributional Distortion:** While we must smooth the sampling probabilities to prevent underfitting small datasets, we want to minimize the distortion of the natural data distribution p_i . Measuring the Kullback-Leibler divergence $D_{\text{KL}}(w_i||p_i)$ shows that \sqrt{N} alters the true data distribution the least.
- **Established Precedent:** This weighting belongs to the exponential smoothing family (N_i^α) established in large-scale multilingual pretraining. While models like XLM-R [9] and mT5 [48] tuned this exponent to $\alpha = 0.3$ to aggressively upsample the long tail, \sqrt{N} ($\alpha = 0.5$) serves as a balanced, parameter-free middle ground.

Empirical Validation. As shown in Table 10, we evaluated all three strategies at the 1.2M parameter scale across the full benchmark. \sqrt{N} -proportional sampling achieves the **lowest overall median VRMSE** (2.85×10^{-2}) and outperforms the baselines on 5 out of 8 datasets. While uniform sampling narrowly minimizes error on the smallest datasets (TRL2D and VI) due to extreme early overfitting, \sqrt{N} provides the robust, balanced signal required for generalized multi-physics training at scale.

Table 10: Ablation of dataset sampling strategies at the 1.2M parameter scale. VRMSE (median) on one-step prediction across eight datasets from The Well benchmark [36]. Best result per dataset in **bold**.

Dataset	S1: Uniform	S2: Temp-Scaled ($T=0.2$)	S3: $\sqrt{\cdot}$-Prop (ours)
AM	6.07e-2	7.18e-2	7.90e-2
GS	8.07e-3	6.19e-3	5.31e-3
ASM	2.79e-2	1.91e-2	1.82e-2
HS	8.48e-3	8.42e-3	7.23e-3
RB	4.82e-2	4.15e-2	3.88e-2
SF	1.27e-2	8.69e-3	8.39e-3
TRL2D	1.80e-1	1.96e-1	2.25e-1
VI	1.79e-1	2.13e-1	2.28e-1
<i>Median (overall)</i>	3.81e-2	3.03e-2	2.85e-2
<i>Dataset wins</i>	3	0	5

G Rollout Finetuning

Autoregressive models accumulate errors over long rollouts: small per-step inaccuracies compound, causing the predicted trajectory to drift increasingly far from the true solution. To address this, we explore several finetuning strategies that expose the model to its own predictions during training, thereby reducing the mismatch between training (teacher-forced) and inference regimes.

We consider four families of methods. **Scheduled Sampling** combines a linear teacher-forcing curriculum with $K=8$ BPTT unrolling: the teacher-forcing rate is annealed from 1.0 to 0.1 over the course of training, progressively replacing ground-truth inputs with model predictions while gradients are backpropagated through the rollout. **BPTT** unrolls the model for K steps and back-propagates through the rollout without any teacher-forcing annealing, evaluated at $K=4$ and $K=8$. **CausalBPTT** [46] runs a fully autoregressive rollout of K steps and weights each step’s loss causally:

$$w_i = \exp(-\epsilon \sum_{k < i} L_k), \tag{10}$$

where L_k is the loss at step k (treated as a constant via `stop_gradient`). At $\epsilon=0$ all steps are equally weighted, recovering plain BPTT. For $\epsilon>0$, step i receives significant gradient only once all earlier steps are well-predicted, implementing a data-driven sequential curriculum without any teacher-forcing annealing. **Pushforward** unrolls K steps but propagates gradients only through the final prediction, detaching intermediate states, also evaluated at $K=4$ and $K=8$.

We evaluate each method on two axes: rollout VRMSE across short (2:8), medium (9:26), and long (27:56) prediction horizons, and one-step prediction metrics to assess degradation from finetuning. The latter is important — aggressive rollout training risks degrading the model’s single-step accuracy, which is undesirable.

Results are shown in Tables 11 and 12. All finetuned methods improve over the baseline at longer horizons, with gains becoming more pronounced as rollout length increases. However, the methods differ substantially in how much they degrade one-step performance. Pushforward incurs the largest one-step penalties across both $K=4$ and $K=8$, with performance worsening as K increases. Notably, BPTT ($K=8$) — which uses the same unroll length as Scheduled Sampling but without annealing — degrades one-step performance considerably, whereas Scheduled Sampling does not. This direct comparison isolates the effect of the teacher-forcing curriculum: gradual annealing allows the model to adapt to its own prediction errors without destabilizing single-step accuracy. Both Scheduled Sampling and CausalBPTT emerge as strong candidates: CausalBPTT achieves competitive rollout performance but at a measurable cost to one-step accuracy, while Scheduled Sampling delivers comparable rollout gains with greater robustness on single-step metrics. We therefore adopt Scheduled Sampling as our rollout finetuning strategy for all subsequent experiments.

Table 11: **Rollout VRMSE (median) by prediction window.** All results on the TRL2D test set. Lower is better. Bold indicates the best value in each column.

Method	Short [2:8]	Medium [9:26]	Long [27:56]
Baseline	0.3797	0.7873	1.0239
Sched. Sampling ($K=8$)	0.3156	0.6544	0.8744
BPTT ($K=4$)	0.3188	0.7107	0.9310
BPTT ($K=8$)	0.3191	0.6457	0.8969
CausalBPTT ($\epsilon=0$)	0.3194	0.6399	0.8774
CausalBPTT ($\epsilon=1$)	0.3147	0.6420	0.8877
CausalBPTT ($\epsilon=5$)	0.3169	0.6588	0.8893
Pushforward ($K=4$)	0.3508	0.6775	0.9003
Pushforward ($K=8$)	0.3713	0.6781	0.9660

Table 12: **One-step prediction metrics.** All results on the TRL2D test set. Lower is better. Bold indicates the best value in each column.

Method	MSE	Rel. ℓ_2	VRMSE (med.)
Baseline	0.03710	0.1134	0.1466
Sched. Sampling ($K=8$)	0.03515	0.1123	0.1505
BPTT ($K=4$)	0.03585	0.1123	0.1487
BPTT ($K=8$)	0.03640	0.1162	0.1595
CausalBPTT ($\epsilon=0$)	0.03623	0.1159	0.1585
CausalBPTT ($\epsilon=1$)	0.03621	0.1151	0.1577
CausalBPTT ($\epsilon=5$)	0.03560	0.1133	0.1528
Pushforward ($K=4$)	0.04257	0.1232	0.1628
Pushforward ($K=8$)	0.04900	0.1340	0.1851

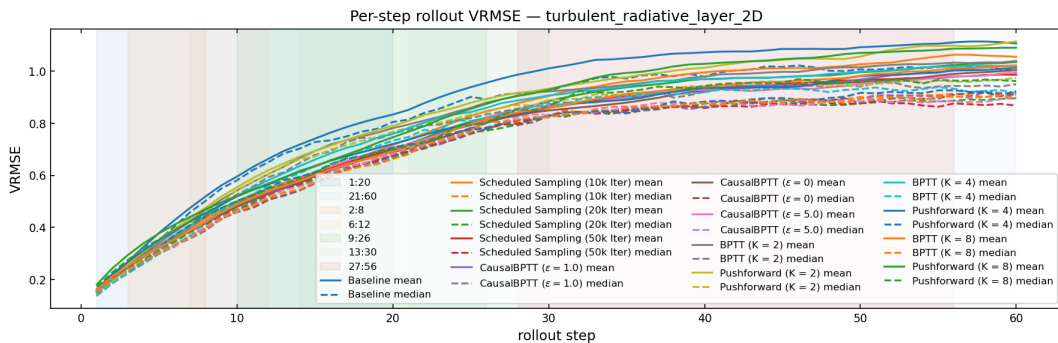


Figure 9: **Median rollout VRMSE as a function of prediction step (TRL2D).** All finetuned methods reduce error accumulation relative to the teacher-forced baseline, with gains widening at longer horizons. Pushforward degrades at both short and long steps as K increases, while Scheduled Sampling and CausalBPTT maintain low error throughout. Shaded bands show the interquartile range over test trajectories.

H Rollout Error Analysis

All autoregressive surrogates trained with teacher forcing share a common failure mode under rollout. We formalize it here and connect it to WaveLiT’s pattern of successes and failures across datasets.

Error recurrence. Let the ground-truth dynamics be governed by $x_{n+1} = f(x_n)$ and the learned map by $\hat{x}_{n+1} = F(\hat{x}_n)$. Starting from a perfect initial condition $x_0 = \hat{x}_0$, define $E_n := \|x_n - \hat{x}_n\|$. Suppose F satisfies:

$$\|f(x) - F(x)\| \leq \epsilon \quad (\text{per-step approximation error}), \quad (11)$$

$$\|F(x) - F(y)\| \leq L_F \|x - y\| \quad (\text{Lipschitz stability condition}). \quad (12)$$

Then:

$$\begin{aligned} E_{n+1} &= \|f(x_n) - F(\hat{x}_n)\| \\ &\leq \|f(x_n) - F(x_n)\| + \|F(x_n) - F(\hat{x}_n)\| \\ &\leq \epsilon + L_F E_n, \end{aligned} \quad (13)$$

and unrolling from $E_0 = 0$ yields

$$E_n \leq \epsilon \sum_{i=0}^{n-1} L_F^i = \begin{cases} \epsilon \frac{L_F^n - 1}{L_F - 1}, & L_F \neq 1, \\ n\epsilon, & L_F = 1. \end{cases} \quad (14)$$

When $L_F > 1$, errors grow geometrically with rollout length, independent of how small ϵ is. Rollout finetuning trains on the rolled-out trajectory and so jointly optimizes ϵ and L_F , in practice trading them off against each other — visible in our experiments as a degradation of one-step accuracy under FT relative to its PT counterpart, in exchange for tighter rollout error within the training horizon. The fundamental constraint is that on chaotic dynamics L_F is bounded below by $e^{\lambda \Delta t}$, where λ is the leading Lyapunov exponent of the underlying flow and Δt is the time step: FT can move along the trade-off curve but cannot escape geometric error growth once the dynamics is genuinely chaotic. When $L_F \leq 1$ the dynamics are contractive and error grows at most linearly in n — long-horizon accuracy is then limited only by ϵ , which a well-matched prior can make small.

I Architectural Ablations

This appendix collects the cumulative ablations that motivate the WaveLiT recipe. Section I.1 isolates the contributions of the wavelet tokenizer and the multiscale feature pyramid, and Section I.2 isolates the contributions of the mixer components.

I.1 Tokenizer and Multiscale Feature Pyramid

To isolate the contribution of each architectural choice, we perform a cumulative ablation on the Navier-Stokes benchmark from PDEArena [13], training all configurations for 200k iterations under identical hyperparameters. Starting from a convolutional encoder-decoder baseline, we incrementally substitute each component and measure both accuracy and wall-clock training time. Results are summarized in Table 13.

Table 13: Cumulative ablation on PDEArena Navier-Stokes (200k iterations). Each row adds one ingredient to the previous configuration. Δ Error denotes relative improvement over the convolutional baseline; higher is better. Δ Time denotes relative change in training time; negative means faster.

Configuration	VRMSE \downarrow	Time	Δ Error	Δ Time
Conv enc/dec (baseline)	0.01172	64.6 min	—	—
Wavelet enc/dec	0.01155	57.4 min	+1.4%	-11%
+ Multiscale (FPN-L1)	0.00968	75.1 min	+17.4%	+16%
+ Multiscale (FPN-L2)	0.00928	84.1 min	+20.8%	+30%
+ Multiscale (FPN-L3)	0.00899	90.0 min	+23.3%	+39%
+ Multiscale (FPN-L4)	0.00897	97.0 min	+23.5%	+50%

Replacing the convolutional encoder-decoder with the wavelet tokenization scheme yields only a modest accuracy improvement (+1.4%) while *reducing* training time by 11%. This is perhaps not surprising, since a convolutional encoder should be able to approximate wavelet-like features over the course of training; the gain we observe is consistent with the findings of [20], who leveraged wavelet tokenizers for pixel-space diffusion models. The more substantial gain comes from introducing multiscale computation via the feature pyramid: a single pyramid level (FPN-L1) reduces error by 17.4% relative to the baseline at a cost of 16% additional training time, and additional levels provide diminishing returns. To keep the training-cost-accuracy frontier balanced, we adopt FPN-L1 as the default for all subsequent experiments.

I.2 Mixer Components

Table 14: Ablation of the proposed mixer design. We keep RoPE fixed in all configurations and progressively add ridge regularization, kernel gating, local positional enhancement (LePE), conditional positional encoding (CPE), and the MILA-style block design. The largest improvements arise from LePE/CPE and the MILA-style block, while ridge regularization and kernel gating provide comparatively modest gains. Comparing B3 and C1 further shows that re-enabling the kernel gate yields only a small additional improvement over the no-gate MILA configuration.

Model	Ridge	Kernel Gate	LePE	CPE	MILA Block	Test/Rel. \downarrow	Runtime \downarrow
A1: RoPE-LA						0.21906	36m 37s
A2: + Ridge	✓					0.20256	39m 30s
A3: + Kernel Gate	✓	✓				0.19236	40m 38s
A4: + LePE	✓	✓	✓			0.11463	40m 56s
A5: + CPE	✓	✓	✓	✓		0.03055	43m 07s
B1: MILA + LePE (no gate)			✓		✓	0.060258	40m 41s
B2: + Ridge (no gate)	✓		✓		✓	0.055471	42m 58s
B3: + CPE (no gate)	✓		✓	✓	✓	0.025324	46m 42s
C1: Full model	✓	✓	✓	✓	✓	0.024363	47m 25s

Table 14 presents an additive ablation of our mixer design. Starting from a RoPE-equipped linear attention baseline (A1), ridge regularization and kernel gating provide only incremental improvements

(A2–A3). In contrast, introducing local positional structure through LePE produces a substantial gain (A4), and adding CPE yields a further large improvement (A5), indicating that positional and locality-aware mechanisms are the dominant contributors in the standard linear-attention branch.

We next evaluate an MILA-inspired branch in which the kernel gate is disabled (B1–B3) in order to isolate the contribution of the MILA-style block design from that of the additional output modulation. This branch consistently outperforms its non-MILA counterpart at comparable levels of positional modeling, and the full no-gate MILA variant (B3) already surpasses the best non-MILA configuration (A5). These results suggest that the MILA-style block design contributes independently beyond the gains obtained from LePE and CPE alone.

Ultimately, each component contributes positively, making the full model (C1) the best overall configuration. The proposed recipe successfully combines two complementary perspectives: the ridge regression view of test-time regression, which motivates the regularization and gating choices, and standard positional and locality augmentations (LePE, CPE), which are critical for the bidirectional spatial setting. While the regression-inspired components provide consistent refinements, the dominant contributors remain the MILA block design and the positional/locality operators, consistent with prior findings in vision settings.

J Detailed Results Tables

All tables below compare WaveLiT bespoke variants (1.2M and 9.5M parameters, pretrained and rollout-finetuned) against four foundation model baselines across eight TheWell benchmarks. Rows marked † indicate checkpoints that diverged under autoregressive rollout and are excluded from ranking. MPP-AViT-L was not evaluated on GS; VI trajectories contain only 16 rollout steps, leaving the $T \in [21:60]$ window undefined for all models.

Table 15: **One-step VRMSE** (median teacher-forcing next-step prediction error, lower is better). Bold = best per dataset. † = diverged checkpoint, excluded from ranking. ASM*: one-step aggregates all sliding-window positions including trivially predictable early steps.

Dataset	Baselines				Ours			
	MPP-AViT-L	Poseidon-L	DPOT-H	Walrus	1.2M-PT	1.2M-FT	9.5M-PT	9.5M-FT
ASM*	0.0337	0.0116	0.0126	0.0099	0.0036	0.0037	0.0016	0.0017
HS	0.0026	0.0019	0.0017	0.0005	0.0003	0.0004	0.0005	0.0005
RB	0.0264	0.0215	0.0288	0.0059	0.0139	0.0159	0.0065	0.0077
SF	0.0071	0.0090	0.0162	0.0012	0.0024	0.0308	0.0015	0.0023
TRL2D	0.1707	0.1323	0.1601	0.0831	0.1421	0.1466	0.1167	0.1186
AM	0.0157	0.0214	0.0476	0.0057	0.0211	0.0282	0.0114	0.0131
GS	—	0.0048	0.0061	0.0001	0.0007	0.0008	0.0006	0.0008
VI	0.1030	0.0878	0.1398	0.0295	0.1084	0.1244	0.0301	0.0336

Table 16: **Short-horizon rollout VRMSE**, $T \in [1:20]$ (median over trajectories of mean autoregressive VRMSE over steps 1–20, lower is better). Bold = best per dataset. † = diverged checkpoint.

Dataset	Baselines				Ours			
	MPP-AViT-L	Poseidon-L	DPOT-H	Walrus	1.2M-PT	1.2M-FT	9.5M-PT	9.5M-FT
ASM	0.0797	0.0785	0.0350	0.0345	0.0239	0.0221	0.0158	0.0153
HS	0.0053	0.0201	0.0022	0.0040	0.0008	0.0009	0.0017	0.0015
RB	0.4109	1.3819	3.4868	0.0992	5.7239	4.0865	1.4417	1.8252
SF	0.0377	0.0657	0.0772	0.0146	0.1375	0.1884	0.0588	0.0657
TRL2D	0.4796	0.4117	0.5134	0.3393	0.5684	0.4540	0.3362	0.3371
AM	0.3195	0.3355	0.5272	0.1262	0.5098	0.4072	0.2096	0.2231
GS	—	0.0411	0.1354	0.0278	0.1086	0.1002	0.0762	0.0824
VI	0.1578	0.1532	0.1989	0.0373	0.4898	0.3340	0.1533	0.1651

Table 17: **Long-horizon rollout VRMSE**, $T \in [21:60]$ (median over trajectories of mean autoregressive VRMSE over steps 21–60; steps 21–46 for HS, lower is better). Bold = best per dataset. † = diverged checkpoint. VI trajectories contain only 16 rollout steps; this window is undefined.

Dataset	Baselines				Ours			
	MPP-AViT-L	Poseidon-L	DPOT-H	Walrus	1.2M-PT	1.2M-FT	9.5M-PT	9.5M-FT
ASM	0.1390	0.2429	0.0543	0.0560	0.1166	0.0693	0.0406	0.0268
HS	0.0096	0.0507	0.0031	0.0074	0.0020	0.0022	0.0047	0.0038
RB	0.7468	0.9586	1.2664	0.6441	2.7116	1.9080	1.1690	1.4803
SF	0.1814	0.2408	0.2880	0.0810	1.0732	0.8311	0.3812	0.2539
TRL2D	0.8879	0.8441	0.9316	0.8648	1.0853	0.8398	0.8759	0.7986
AM	1.2481	1.3015	1.2867	1.2451	1.4186	1.3863	1.3016	1.3204
GS	—	0.1295	0.6567	0.1268	0.4045	0.3996	0.3040	0.3048
VI	—	—	—	—	—	—	—	—

Foundation Model: Detailed Comparison

Tables 19–21 compare WaveLiT-FM against Walrus and the best bespoke WaveLiT variant per cell. The *Best WaveLiT* column reports the minimum across all four bespoke variants (1.2M-PT/FT, 9.5M-PT/FT). ‡ marks cells where a foundation model variant beats Walrus. † marks rollout divergence.

Table 18: **Average per-dataset rank** across the eight TheWell benchmarks (lower is better). Each model’s rank is computed within each dataset; ties get the mean rank; undefined cells are excluded (MPP-AViT-L on GS for all windows; VI for long-horizon). WaveLiT rows use the better of pretrained and rollout-finetuned variants per cell, matching Figure 4. WaveLiT-9.5M is the runner-up to Walrus in every window despite being $\sim 130\times$ smaller.

Model	Params	One-step	$T \in [1, 20]$	$T \in [21, 60]$
Walrus	1.2B	1.44	1.75	2.14
WaveLiT-9.5M	9.5M	1.94	2.38	3.00
WaveLiT-1.2M	1.2M	3.12	4.25	4.14
Poseidon-L	629M	4.12	3.62	3.86
MPP-AViT-L	409M	4.86	3.86	3.50
DPOT-H	$\sim 1B$	5.38	4.88	4.00

Table 19: **One-step VRMSE** — foundation model results in context. Bold = best per dataset across all four columns. ‡ = foundation model beats Walrus.

Dataset	Walrus (external)	Best WaveLiT (bespoke)	Fnd-PT (multi-task)	Fnd-FT (multi-task + FT)
ASM	0.0099	0.0016	0.0087‡	0.0097‡
HS	0.0005	0.0003	0.0057	0.0061
RB	0.0059	0.0065	0.0171	0.0198
SF	0.0012	0.0015	0.0046	0.0069
TRL2D	0.0831	0.1167	0.1508	0.1655
AM	0.0057	0.0114	0.0423	0.0540
GS	0.0001	0.0006	0.0032	0.0039
VI	0.0295	0.0301	0.0970	0.1100

Table 20: **Short-horizon rollout VRMSE**, $T \in [1 : 20]$. † = Fnd-PT diverges on RB under autoregressive rollout (value shown for completeness, excluded from ranking).

Dataset	Walrus (external)	Best WaveLiT (bespoke)	Fnd-PT (multi-task)	Fnd-FT (multi-task + FT)
ASM	0.0345	0.0153	0.0429	0.0494
HS	0.0040	0.0008	0.0179	0.0183
RB	0.0992	1.4417	5.7242†	4.6113†
SF	0.0146	0.0588	0.1376	0.1091
TRL2D	0.3393	0.3362	0.6729	0.5181
AM	0.1262	0.2096	0.7456	0.7195
GS	0.0278	0.0762	0.1964	0.2222
VI	0.0373	0.1533	0.3497	0.2852

Table 21: **Long-horizon rollout VRMSE**, $T \in [21 : 60]$. VI trajectories contain only 16 rollout steps; this window is undefined (—). ‡ = foundation model beats Walrus.

Dataset	Walrus (external)	Best WaveLiT (bespoke)	Fnd-PT (multi-task)	Fnd-FT (multi-task + FT)
ASM	0.0560	0.0268	0.1050	0.0765
HS	0.0074	0.0020	0.0349	0.0346
RB	0.6441	1.1690	2.9770	2.4407
SF	0.0810	0.2539	0.9487	0.5143
TRL2D	0.8648	0.7986	1.1706	0.8471‡
AM	1.2451	1.3016	1.4208	1.3440
GS	0.1268	0.3040	0.6371	0.7173
VI	—	—	—	—

Table 22: Rank-1 finishes across 20 dataset–window pairs (among {Walrus, MPP-AViT-L, Poseidon-L, DPOT-H, Fnd-PT, Fnd-FT}); GS excluded entirely since MPP-AViT-L is not evaluated on it, and VI excluded at $T \in [21:60]$).

Model	Rank-1 count (of 20)
Walrus (1.2B, bespoke)	15
Fnd-FT (10M, multi-task + FT)	0
Fnd-PT (10M, multi-task)	1
DPOT-H	3
Poseidon-L	1
MPP-AViT-L	0

K Comparison with Wavelet Neural Operator

Wavelet-based methods for neural PDE solvers span three distinct families, and it is worth clarifying how WaveLiT relates to each before presenting comparisons:

- **WNO** [40] is an integral kernel method that performs kernel integration directly in the wavelet domain — the wavelet transform defines the space in which convolution is computed, analogous to how FNO operates in the Fourier domain.
- **WDNO** [21] is a diffusion-based generative model that learns to denoise PDE trajectories in the wavelet domain.
- **WaveLiT** uses the DWT as a parameter-free tokenization scheme that feeds a transformer backbone, and reuses the wavelet domain as an auxiliary loss to enforce spectral fidelity. The wavelet transform is not the computational substrate of the operator; it is the input representation.

A direct comparison is therefore not perfectly fair, but it is nonetheless informative. We run WNO using the official repository² with default hyperparameters, adapting only the output dimensionality and spatial resolution to match each benchmark. This yields a WNO model of approximately 9M parameters, directly comparable in size to WaveLiT-9.5M.

Table 23: One-step VRMSE comparison between WNO (~9M parameters) and WaveLiT-9.5M on two TheWell benchmarks. Lower is better. WNO uses default repository settings; WaveLiT-9.5M uses the pretrained checkpoint.

Benchmark	WNO (~9M)	WaveLiT-9.5M
Active Matter	0.5736	0.0114
Turbulent Radiative Layer	0.3939	0.1167

WaveLiT-9.5M outperforms WNO by a large margin on both benchmarks despite identical parameter counts.

²<https://github.com/TapasTripura/WNO/tree/main/Version%202.0.0>